Soft Matter

PAPER

View Article Online
View Journal | View Issue

Check for updates

Cite this: *Soft Matter*, 2019, **15**, 5116

Mapping the phase behavior of coacervate-driven self-assembly in diblock copolyelectrolytes

Gary M. C. Ong[a] and Charles E. Sing *[ab]

Received 12th April 2019,
Accepted 6th June 2019

DOI: 10.1039/c9sm00741e

rsc.li/soft-matter-journal

Oppositely-charged polymers can undergo an associative phase separation process known as complex coacervation, which is driven by the electrostatic attraction between the two polymer species. This driving force for phase separation can be harnessed to drive self-assembly, *via* pairs of block copolyelectrolytes with opposite charge and thus favorable coulombic interactions. There are few predictions of coacervate self-assembly phase behavior due to the wide variety of molecular and environmental parameters, along with fundamental theoretical challenges. In this paper, we use recent advances in coacervate theory to predict the solution-phase assembly of diblock polyelectrolyte pairs for a number of molecular design parameters (charged block fraction, polymer length). Phase diagrams show that self-assembly occurs at high polymer, low salt concentrations for a range of charge block fractions. We show that we qualitatively obtain limiting results seen in the experimental literature, including the emergence of a high polymer-fraction reentrant transition that gives rise to a self-compatibilized homopolymer coacervate behavior at the limit of high charge block fraction. In intermediate charge block fractions, we draw an analogy between the role of salt concentration in coacervation-driven assembly and the role of temperature in χ-driven assembly. We also explore salt partitioning between microphase separated domains in block copolyelectrolytes, with parallels to homopolyelectrolyte coacervation.

1 Introduction

Complex coacervation occurs when two oppositely-charged polyelectrolytes undergo an associative phase separation in an aqueous, salt solution to form a polymer-dense 'coacervate' phase and a polymer-dilute 'supernatant' phase.[1–4] This association is sensitive to environment (*e.g.*, salt concentration,[5–8] pH,[5,9] temperature[5]) and molecular features (*e.g.*, linear charge density, salt valency and identity,[6,10,11] charge sequence,[12,13] stereoregularity,[14,15] architecture,[16] polymer stiffness and charge density,[17] and stoichiometry[5,6,18]); consequently, coacervation has become an important motif for solution self-assembly.[19–23] Oppositely-charged polyelectrolytes can be incorporated into block copolymers (see schematics in Fig. 1), where electrostatic complexation can drive self-assembly into a number of nano-scale structures.[19–25] There has been considerable effort, for example, in using such systems to create 'coacervate core micelles'[19,21,26–28] that are useful as drug delivery vehicles due to their aqueous core being able to carry hydrophilic cargo and their responsiveness to environmental stimuli.[19–21,29]

The utility of coacervate-driven block copolyelectrolyte (BCPE) self-assembly has prompted a number of experimental efforts to map phase diagrams,[23,25,30] to ascertain the molecular and environmental conditions where self-assembly is observed. Examples include salt *versus* polymer phase diagrams for pairs of both di- and tri-block copolyelectrolytes,[23] and a triblock polyelectrolyte phase diagram for different charge fractions at the limit of zero salt.[25,30] However, there are only a few initial forays into a broader BCPE parameter space, because these phase diagrams require extensive experimental effort[23,25,31,32] and may need long equilibration times due to kinetic trapping.[22,24,31,32]

Theoretical prediction could be a powerful tool for determining phase behavior and understanding the physical principles governing coacervate-driven self assembly, complementing experimental efforts. However, there are only a few examples where theory and simulation has been used to understand coacervate-based self-assembly, including a modified self-consistent field theory (SCFT) approach from Audus *et al.*[25] and a scaling theory for micelles from Rumyantsev *et al.*[33] These theories provide insights specific to certain areas of parameter space; Audus *et al.* considers a no-salt limit,[25] and Rumyantsev *et al.* considers micellization at the low-polymer concentration limit.[33] These previous approaches are most accurate in the limit of low linear charge density.[25,33] There remains significant need for phase diagram prediction for high charge density polymers,

[a] *Department of Chemical and Biomolecular Engineering, 600 S. Mathews Ave., Urbana, IL, USA. E-mail: cesing@illinois.edu*
[b] *Beckman Institute for Advanced Science and Technology, 405 N. Mathews Ave., Urbana, IL, USA*

Published on 06 June 2019. Downloaded by University of Illinois - Urbana on 1/28/2020 3:37:06 PM.

This journal is © The Royal Society of Chemistry 2019

Published on 06 June 2019. Downloaded by University of Illinois - Urbana on 1/28/2020 3:37:06 PM.

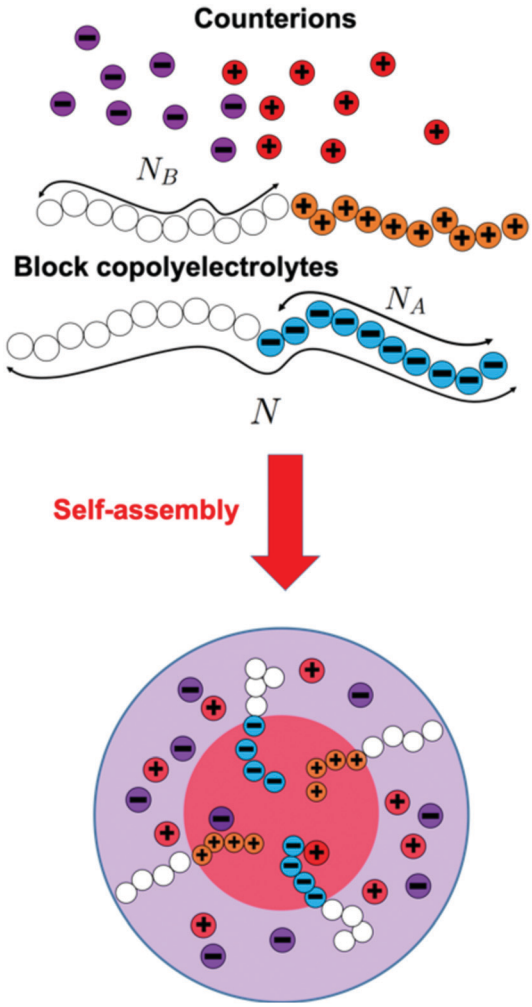

Fig. 1 Schematic of the BCPE system considered in this manuscript; the polymer species at volume fraction ϕ_P consists of oppositely-charged block copolymers, each with N monomers (N_A charged, N_B neutral). We denote different polymer charge fractions/lengths by labelling them as N_A/N_B. The charged species volume fraction is ϕ_S. The salt and block copolyelectrolyte species, in aqueous solution, can undergo self-assembly into micelles (shown) and other nanostructures due to the coacervate-based attraction between oppositely-charged blocks.

with variation in the full parameter space of charge fraction, salt concentration, and polymer concentration.

This dearth of simulation or theory phase diagrams is in stark contrast to neutral block copolymers, where such predictions have been around for decades.[34–36] Even modeling the theoretical phase behavior for a homopolyelectrolyte coacervate system remains a current challenge.[4] Here, most recent work has focused on overcoming the limitations of the original Voorn–Overbeek model for coacervation,[37,38] which is known to neglect key physical aspects of coacervation.[39–41] A diverse range of techniques have been employed, including field theories evaluated computationally[25,42–47] and analytically,[48–54] as well as liquid state theory,[18,39,55,56] scaling arguments,[33,57–59] and an assortment of other approaches.[60–63] There are tradeoffs associated with all of these methods, discussed at length elsewhere,[4,64] but most have difficulty accurately capturing the local, molecular charge correlations in coacervates.[4,65]

We have used coarse-grained, particle-based simulation to demonstrate the importance of molecular features that govern these charge correlations.[12,16,40,66,67] Linear charge density,[39,40] excluded volume,[39,40,67] chain architecture,[16] chain stiffness,[66] and monomer sequence[12,13] can all affect coacervate phase behavior. These simulations have informed the development of a transfer matrix (TM) theory,[66–68] that accounts for charge correlations by keeping track of neighboring, paired charges.[66–68] This is a formalization of ion pairing and counterion condensation and release ideas that play a large role in the thermodynamics charged pair complexes[61,69–76] and multivalent-driven polyelectrolyte precipitation,[77–80] and can be incorporated into standard SCFT calculations and nearly quantitatively compared to inhomogeneous coacervate/supernatant interfaces in full particle-based simulations.[67]

In this paper, we use this new TM-SCFT method to calculate the phase behavior of self-assembled structures in coacervate-driven diblock copolyelectrolytes to predict the phase behavior for BCPEs.[66–68] We show that phase diagram predictions calculated by TM-SCFT qualitatively reproduce or are analogous to experimental results in the literature,[23,81–83] and show how these trends are affected by molecular and environmental parameters such as the charge block fraction, molecular weight, salt concentration, and polymer concentration. Features unique to coacervate-driven assembly are also observed such as salt partitioning between the phase-separating domains.

2 Methods

We consider a system of two oppositely-charged BCPEs that each have a charged block A and an uncharged block B (see schematic in Fig. 1). The two BCPE species are assumed to be identical, and in stoichiometric charge balance, such that they are treated as the same species of A–B block copolymers. This BCPE has N_A charged monomers and N_B uncharged monomers, along its overall degree of polymerization $N = N_A + N_B$. Salt S is included in our model, and cations and anions are also assumed to be equivalent and in stoichiometric charge balance, and can be represented as a single species. Finally, water W is included as a third species. This work thus considers solutions of oppositely-charged BCPE pairs, with different values of the block lengths N_A/N_B; we will characterize their phase behavior in a parameter space of polymer volume fraction ϕ_P and salt volume fraction ϕ_S.

The TM-SCFT method is described in detail in Lytle *et al.*,[67] and is outlined in detail in the appendix of this article. This method combines a molecular theory of coacervation (the transfer-matrix theory, TM) and the self consistent field theory (SCFT) model of polymer self-assembly. The TM theory maps the local, correlated charged interactions in the system to a one-dimensional adsorption model; here, a test polyelectrolyte serves as connected sites upon which the oppositely-charged species (polyelectrolyte and small-molecule species) can adsorb

Published on 06 June 2019. Downloaded by University of Illinois - Urbana on 1/28/2020 3:37:06 PM.

and 'pair' the charges.[66–68] The statistics of this adsorption is set by the state of the system, as determined by the volume fractions ϕ_j of all species j = A, B, S, W, and incorporates electrostatics *via* an energy penalty for un-paired charges. This model can be calculated either numerically[66] or sometimes analytically[67,68] using the transfer matrix approach, to capture the local charged interactions that determine coacervate thermodynamics with a free energy of interaction $\tilde{f}_{TM}(\{\phi_j(\mathbf{r})\})$ that is a function of the volume fraction $\phi_j(\mathbf{r})$ at a given position $\mathbf{r}$:[66–68]

$$\tilde{f}_{TM}\left(\left\{\phi_j(\mathbf{r})\right\}\right) = -\frac{\phi_A}{2N}\ln\left[\vec{\psi}_0^T\mathbf{M}^N\left(\left\{\phi_j(\mathbf{r})\right\}\right)\vec{\psi}_1\right] + \zeta(\Lambda(\phi_A+\phi_B)+\phi_S)^3 \quad (1)$$

This interaction free energy is built around a transfer matrix $\mathbf{M}$ (described explicitly in the appendix) that captures the Boltzmann factors of increasing the size of a polyelectrolyte 'test chain' whose monomers interact with nearby chains and salt ions of opposite charge.[68] The vector $\vec{\psi}_1$ is comprised of Boltzmann factors for the first monomer in this chain, and $\vec{\psi}_0$ is a vector of ones.[68] We consider the TM theory to be one of a larger class of ion pairing-based models[61,62,84] with our model specifically accounting for both the connectedness of polymers and the local charge correlations in a way that can be compared directly with particle-based simulations of coacervation.[66,68] Our model is distinguished from other works by including a phenomenological third-order term (the second term in eqn (1)) that accounts for the excluded volume/packing of species in the dense coacervate phase. The parameters ζ = 19.0 and Λ = 0.6875 are used consistently across a number of previous works, with the latter reflecting the difference in hard-core excluded volume for free ions and connected polymer charges.[66–68] Kudlay and Olvera de la Cruz first recognized the importance of including this excluded volume effect,[51] confirmed later by our work on liquid-state theory[39] and particle-based simulation.[40] Key elements of these simulation and theory predictions were confirmed with experiments.[40] More recent simulation work using explicit solvent has also seen similar effects.[41]

We incorporate the local TM-based free energy expression into an SCFT Hamiltonian that accounts for polymer self-assembly length scales, and is a functional of the species volume fraction fields $\phi_j(\mathbf{r})$ and their auxiliary fields $W_i(\mathbf{r})$:[67,85–88]

$$\mathscr{H}\left[\left\{\phi_j\right\},\left\{W_j\right\}\right] = -n_P\ln Q_P[W_A,W_B] - n_S\ln Q_S[W_S] - n_W\ln Q_W[W_W] + \rho_0\int d\mathbf{r}\left[\tilde{f}_{TM}\left(\left\{\phi_j(\mathbf{r})\right\}\right).\right.$$
$$\left.+\frac{\zeta}{2}\left(\sum_k\phi_k-1\right)^2-\sum_k W_k(\mathbf{r})\phi_k(\mathbf{r})\right] \quad (2)$$

ζ is a large constant, and its corresponding term constrains the system such that the sum of the volume fractions is equal to one.[67,87,88] ρ_0 is the number density of all species, n_i is the number of molecules of species i, and b is the length of a single polymer segment. The single-particle partition functions for the small molecule species i = S, W are given by $Q_i = V^{-1}\int d\mathbf{r}\exp(-W_i(\mathbf{r}))$.[85] The single-chain partition function for the polymers $Q_P[W_A,W_B]$ is given by $Q_P[W_A,W_B] = V^{-1}\int d\mathbf{r} q_P(\mathbf{r},N[W_A,W_B])$,[85] where q_P is the propagator that is described by a diffusion equation:[85]

$$\frac{\partial q_P(\mathbf{r},s[W_A,W_B])}{\partial s} = \frac{b^2}{6}\nabla q_P(\mathbf{r},s[W_A,W_B]) - W_i q_P(\mathbf{r},s[W_A,W_B]) \quad (3)$$

This equation can be solved numerically by calculating how q_P changes along the contour coordinate of the chain $0 < s < N$.[85] The initial condition for a discrete chain with $s = 0$ representing the initial monomer is $q_P(\mathbf{r},0;[W_A,W_B]) = \exp(-W_i)$, and $W_i = W_A$ for $s < Nf_A$ and $W_i = W_B$ for $s \geq Nf_A$. This modified diffusion equation is solved by the finite difference method, with a contour step size of Δs = 1.0, and with a box size of 45 × 45 (in units of b). SCFT determines the saddle point of the Hamiltonian, which occurs when the functional derivatives of the Hamiltonian with respect to the fields are zero, *i.e.*, $(\delta\mathscr{H}/\delta\phi_j(\mathbf{r}))_{\phi_j^*} = 0$ and $(\delta\mathscr{H}/\delta W_j(\mathbf{r}))_{W_j^*} = 0$. This procedure is well described in the literature.[85,89]

Our previous work has demonstrated the ability of the TM-SCFT method to reproduce density profiles in particle-based simulations of inhomogeneous coacervate systems.[67] This includes in the presence of neutral polymers, such as in the charged and neutral blocks of the block copolyelectrolytes we are studying here.[67] Nevertheless, we note that a number of approximations present in both the TM portion and its incorporation into SCFT, beyond the standard assumptions known in standard SCFT.[85] First, the TM theory assumes a mean-field environment of polyelectrolytes and small molecule ions, not accounting for correlations beyond ion-pairing interactions. We justify this approximation by appealing to the short-range correlations observed in simulation,[40] which are dominated by neighbor peaks in the pair correlation functions; nevertheless, this will break down in the dilute solution limit that is not the focus of this work. We expect the suitability of this mean-field assumption to be approximately quantified by the same type of Ginzburg parameter $C = n_P R_{g0}^3/V$ that dictates the validity of the analogous mean-field assumption in the underlying SCFT model, which is the number of chains in a volume set by the unperturbed radius of gyration of the polymer.[85]

We further note that the TM model introduces electrostatics *via* an energetic penalty for un-paired ions, that is assumed to be concentration independent. This theory is thus most accurate in the high charge-density limit, characterized by strong ion pairing to the polyelectrolytes. Our previous efforts have shown that this approach can be extended to charge fractions as low as f_C = 0.4,[13] though at increasingly low charge fractions we expect scaling[33,57–59] or field theoretic methods[25,42–47] to become more suitable. Indeed, we briefly note that our TM-SCFT method is analogous to previous work by Audus *et al.*,[25] in that a thermodynamic model of charge correlations is incorporated into SCFT to understand coacervate-driven self-assembly. In this manuscript, the TM model is used to capture a local excess free energy due to

 This journal is © The Royal Society of Chemistry 2019

Published on 06 June 2019. Downloaded by University of Illinois - Urbana on 1/28/2020 3:37:06 PM.

correlations, and is specifically developed for high charge-density polymers.[66–68] Audus *et al.*[25] instead use the one-loop approximation of the polyelectrolyte field theory,[48,49,51–53] which is most accurate for low charge-density polymers.

We also do not include dielectric effects that may arise in dense solutions of polymers considered here.[86,90–92] Incorporation of TM into SCFT assumes a separation of length scales, treating charge correlations as local to a given SCFT grid point *via* a 'local homogeneity' ansatz discussed in our prior work.[67] Nevertheless, prior successful comparison of this method to simulation and experiment[67] – which do not carry the main assumptions of the TM-SCFT – suggest that we can describe inhomogeneous coacervate systems such as coacervate-driven self-assembly.

3 Results

We can apply the TM-SCFT method to determine the self-assembly behavior of charge-neutral block copolymers. We begin by studying the two-dimensional phase behavior of oppositely-charged block copolyelectrolytes, to show broad trends in molecular features such as charge fraction and degree of polymerization. We further demonstrate that the effective three-component system leads to non-uniform salt partitioning, and finally show that our approach can be extended to three dimensions.

3.1 Two-dimensional phase diagrams

Fig. 2 shows some characteristic morphologies seen in our calculations. We primarily focus exclusively on two-dimensional SCFT calculations, because this limits the number of possible morphologies we could observe while still capturing important trends and qualitative locations of order–disorder and order–order transitions. We observe a disordered phase (D), a micelle phase (M), an ordered hexagonal phase with an A-block core (H) and its inverse with a B-block core (I), and finally a lamellar phase (L). We observe H, I, and L as single phases, and not in coexistence with each other or with a supernatant. We can also observe a bulk coacervate phase (C) that forms a single region of coacervate (often a droplet) within a supernatant phase, that is significantly larger than the other nanophase separated morphologies observed in Fig. 2.

3.1.1 The effect of charge block ratio. We map the coacervate-driven self-assembly of BCPEs in Fig. 3, for a constant value of N = 60 and a number of charge block ratios (denoted as N_A/N_B). Each charge ratio is separately plotted on a phase diagram of salt concentration ϕ_S *versus* polymer concentration ϕ_P. We characterize morphologies using visual observation, with relatively large box sizes $\left(L \gg \sqrt{N}b\right)$ to minimize finite-size effects. The boundaries between phases are calculated by first determining the mean-field free energy associated the value of $\mathscr{H}^*$ given in eqn (2) at the saddle point for each candidate morphology. A surface $\mathscr{H}^*(\langle\phi_P\rangle,\langle\phi_S\rangle)$ for each possible morphology is generated, and the intersections serve as the transitions between morphologies. In Fig. 3e, constant – ϕ_P and ϕ_S slices are used instead of surfaces, due to practical limitations arising from the small phase regions. We note that direct observation of SCFT results generated from random initial fields are consistent with these predictions, which we use to characterize two of the boundaries we include in Fig. 3. The boundary between the D and M phase is given by the lowest overall polymer concentration where we observe the micelle phase, which we note is not a precise determination of the critical micelle concentration.[28,33,34,93] We expect it to be much lower due to finite size effects, and thus denote this boundary with dotted lines. We also use direct visual observation to characterize the M to H transition, due to the practical challenges associated with accurately calculating the micellar translational entropy contribution to the M free energy $\mathscr{H}^*$.[34]

In the limit of low charge fraction (Fig. 3a, 10/50 system), the TM-SCFT phase diagrams is qualitatively comparable with an experimental phase diagram given in Krogstad *et al.*,[23] for diblock BCPE systems. Here, the disordered-to-ordered transition is observed to occur at a relatively high volume fraction of polymers, and quickly becomes disordered with increasing salt ϕ_S. Mapping the location of 3-D morphologies is not the focus of this work, hence we do not compare the location of the BCC morphology to the experimental phase diagram.[23] We will,

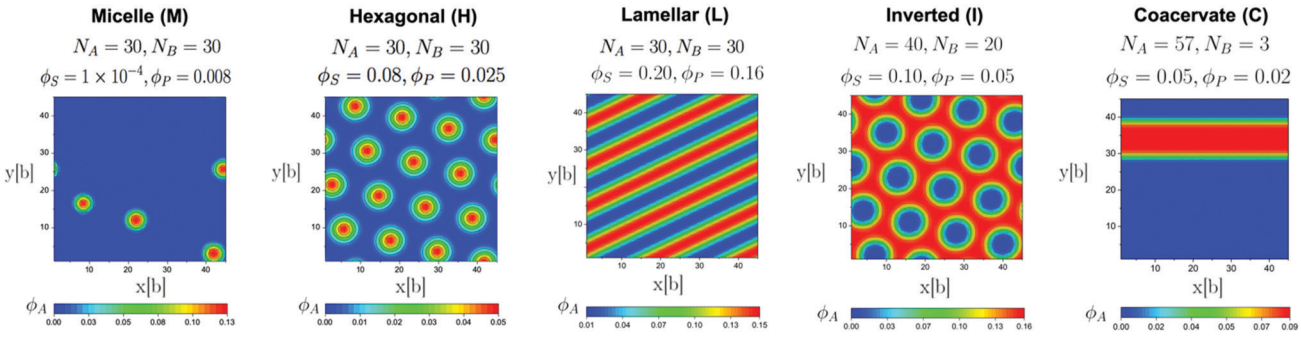

Fig. 2 Representative contour plots of the morphologies observed in two-dimensional TM-SCFT calculations, showing the density of the polyelectrolyte block ϕ_A. We observe micelle phases (M), hexagonally-packed micelles (H), lamellar (L), and inverse hexagonally-packed micelles (I) as self-assembled phases. We also occasionally observe bulk phase separation into a coacervate phase (C), distinguished as a phase separated region that is significantly larger than the H or M structures.

Published on 06 June 2019. Downloaded by University of Illinois - Urbana on 1/28/2020 3:37:06 PM.

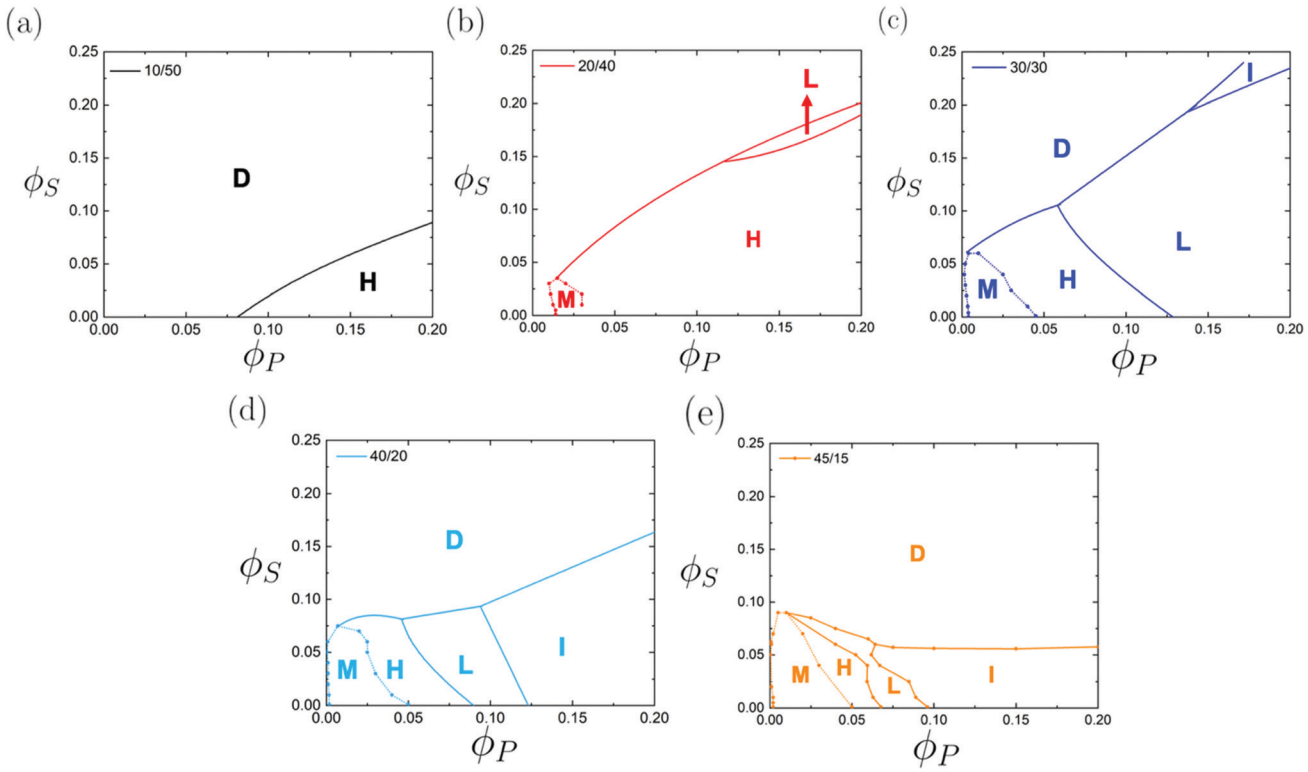

Fig. 3 Salt concentration ϕ_S *versus* polymer concentration ϕ_P phase diagrams for N = 60 with increasing charge fraction; (a) 10/50 (b) 20/40 (c) 30/30 (d) 40/20 (e) 45/15. Letters denote morphologies described in Fig. 2. We note the general trend is that there is a transition from H to L to I as ϕ_P and charge block fraction is increased, which is consistent with results for uncharged block copolymers.[81–83] The disordered phase D also initially shrinks in (a–c) due to the increase in charge block fraction, but begins to increase in (d and e) as the block copolyelectrolyte block fraction approaches the limiting case for homopolymer coacervates.

however, show proof-of-principle for extension of this method to 3-D calculations in Section 3.4.

For low charge-fraction BCPEs (Fig. 3a–d), self-assembly generally occurs at high ϕ_P and low ϕ_S, where the electrostatic interactions are sufficiently un-screened to overcome the translational entropy lost by the polymer upon forming self-assembled structures. The strength of these interactions generally increases with N_A due to the increased number of charges per chain, leading to a shifting of the order–disorder transition to higher ϕ_S and lower ϕ_P for most f_A. The order–order transitions similarly shift to lower values of ϕ_P as f_A is increased, in analogy to standard block copolymer assembly,[82,94,95] which sets transitions from H to L to I as the relative volume of the A phase is increased.

After an initial decrease in ϕ_P and increase in ϕ_S for the order–disorder transition as N_A increases, we note that it begins to move the opposite direction, such that the size of the D region increases at high ϕ_P and ϕ_S proceeding from 30/30 to 40/20 (Fig. 3c and d). This continues into the 45/15 (Fig. 3e), where the D region now encompasses most of the high ϕ_P, high ϕ_S portion of the phase diagram.

3.1.2 Bulk coacervation at high charge fractions. At very high values of $N_A > 45$, there is a disappearance of nanophase separation in the non-D portion of the diagram, where now the system simply forms a bulk coacervate phase C (as shown in Fig. 2). Here, the system approaches the limit where the chains are fully charged, and thus exhibit standard homopolymer coacervation;[2,7] in this case, the charged blocks are long enough to incorporate the small homopolymer blocks directly into the bulk phase separation. We plot a number of these phase diagrams in Fig. 4a, for 50/10, 57/3, and finally for the homopolymer case 60/0. We note that the presence of the neutral block suppresses phase separation, which otherwise behaves similarly to coacervation phase diagrams in the literature.[2–4]

Outside of the bulk phase behavior, the blocky nature of the 50/10 and 57/3 polymers also exhibit interesting interfacial behavior. To show this, we plot one-dimensional calculation of coacervation of this series of block copolymers in Fig. 4b. There is the formation of a clear bulk phase for all polymers in this series, however there are distinct differences in the interface between the supernatant and coacervate. This is most apparent for 50/10, which shows peaks at the interface for both ϕ_A and ϕ_B. The neutral ϕ_B locally partitions to the polymer-dilute supernatant phase, which is consistent with the expulsion of neutral polymers from coacervates observed in our previous work.[67] This enriches the neutral block at the interface, which is connected to the charged block ϕ_A; this charged block shows a density peak on the coacervate-side of the interface. The block copolymer, while it does not microphase separate, appears to thus compatibilize the interface between

 This journal is © The Royal Society of Chemistry 2019

Published on 06 June 2019. Downloaded by University of Illinois - Urbana on 1/28/2020 3:37:06 PM.

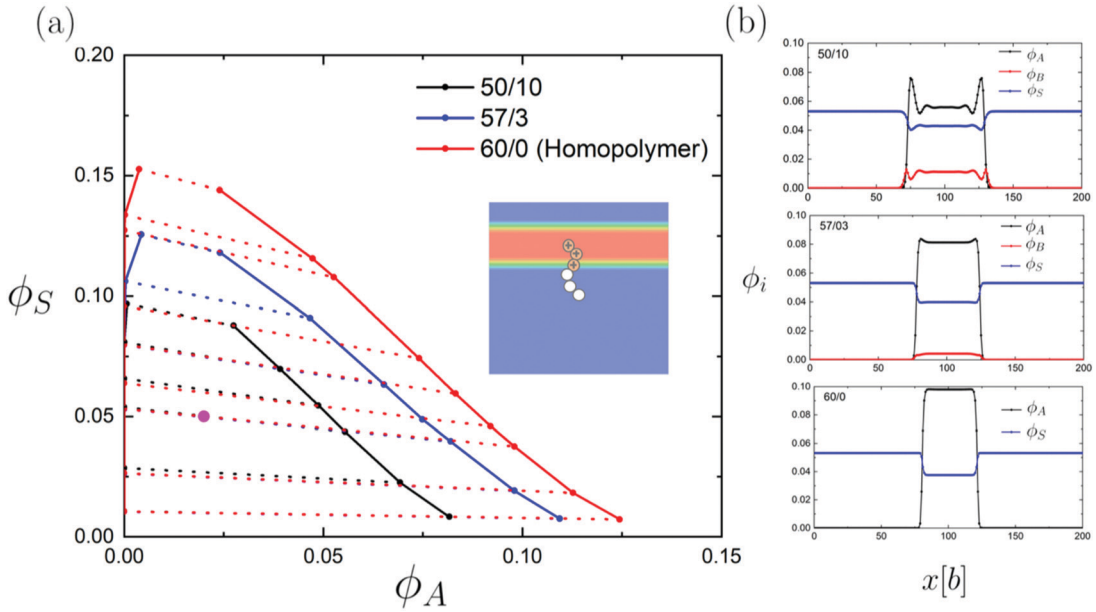

Fig. 4 (a) Salt concentration ϕ_S *versus* polymer concentration ϕ_P phase diagrams for N = 60 with large charge block fractions; 50/10, 57/3, and 60/0; the last of these sequences is the homopolymer coacervate limit. All of these polymer species undergo a macroscopic phase separation characteristic of bulk coacervation, with the small, uncharged block being incorporated into the coacervate. Tie-lines denote coexisting phases. Inset shows the contours from Fig. 2, indicating the relative placement of the block copolymers at the interface between the coacervate and supernatant. Block copolymer shown is only for schematic purposes; degree of polymerization is not reflective of parameters for this profile, which is for a 57/3 diblock. (b) Density profiles from 1-D TM-SCFT calculations of these polymers at the point in (a) denoted by the magenta dot, showing that the presence of compatibilization at the interface between the coacervate and supernatant. These manifest as marked density peaks, with the neutral block at the edges of the coacervate phase that 'dangle' into the supernatant, leading to a local increase in charged block density on the coacervate side of the interface. These peaks disappear as the neutral block shrinks, until for the homopolymer case (60/0) the interface smoothly varies between the two phases, as has been reported previously.[67]

the bulk coacervate and supernatant phases. We schematically show this in the inset of Fig. 4a. This is seen at 57/3 as well, however only slightly, and this effect disappears for a homopolymer (60/0).

3.1.3 The effect of chain length. In analogy to homopolyelectrolyte coacervates, where a longer chain length has been shown to increase the size of the phase separated region,[7,41] block copolyelectrolyte assembly is enhanced by increasing the length of the charged block independently of the charge fraction. We show this in Fig. 5, which plots ϕ_S *versus* ϕ_P phase diagrams for a variety of overall N for $N_A = N_B$. There are a number of differences in the phase behaviors as chain length is increased from N = 30–80, but importantly the primary difference is that the order–disorder transition increases to higher salt concentrations ϕ_S. We attribute this to the increased number of charged interactions per chain, and thus increased electrostatic driving force to compete against the chain translational entropy. Nevertheless, the charge fraction remains the same (50%), so the relative balance of the chain coil sizes leads the molecules to form similar morphologies regardless of N. We also note that, at the limit of large N = 60, 80 (Fig. 5d and e), there is relatively little change in the phase behavior compared to a similar range of N = 30–50 (Fig. 5a–c). We attribute this to approaching what is analogous to a 'strong segregation' limit, similar to that found in standard χ-driven block copolymer assembly;[96] here, the chain length approaches a large-N limit where self-assembly is due solely to chain length-insensitive properties such as the relative chain swelling between A and B blocks and the equilibrium domain densities.

3.2 Connection to experimental observations

We can qualitatively compare coacervate-driven BCPE phase behavior to the experimental and theoretical observations for χ-driven self-assembly of uncharged BCPs.[81,82] For BCPEs, the salt concentration has an analogous effect to temperature and the extent of solvent 'selectivity' towards one block of the BCP. In χ-driven self-assembly of BCPs, as temperature increases, the short range selectivity or solvophobic interactions decrease in strength relative to the thermal energy.[95,97] In most cases, an increase in T results in a weakening of solvophobicity, decreasing the tendency toward phase separation.[81,82] Similarly in BCPEs, an increase in salt concentration diminishes the electrostatic attractions between oppositely charged polyelectrolytes which results in a decrease in the driving force for coacervation and thus phase separation. We note that the intermediate charge fractions for 30/30 and 40/20, in Fig. 3c and d respectively, exhibit phase boundaries that qualitatively correspond to three-dimensional counterparts observed in classical experimental phase diagrams in the experimental and theoretical literature.[81–83,98,99]

3.3 Salt partitioning

In addition to showing the morphologies observed as a function of the polyelectrolyte block concentration ϕ_A in Fig. 2,

Published on 06 June 2019. Downloaded by University of Illinois - Urbana on 1/28/2020 3:37:06 PM.

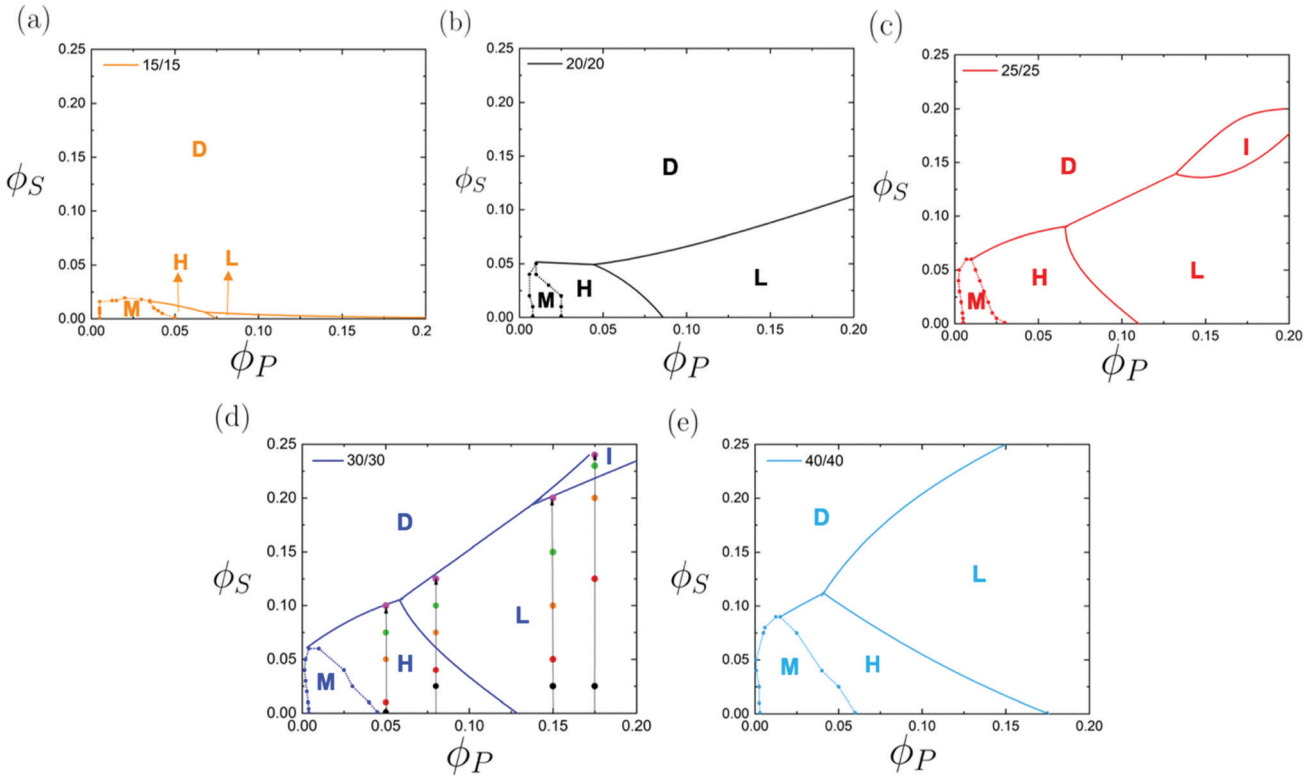

Fig. 5 Salt concentration ϕ_S *versus* polymer concentration ϕ_P phase diagrams for $N_A = N_B$ with increasing polymer length N; (a) 15/15 (b) 20/20 (c) 25/25 (d) 30/30 (e) 40/40. Letters denote morphologies described in Fig. 2. We note the order–disorder transition salt concentration ϕ_S increases noticeably with N, but yet the morphologies observed remain essentially the same. Non-phase boundary points in (d) correspond to SCFT calculations carried out to provide salt partitioning data in Fig. 6.

we also consider the distribution of small molecule salt ϕ_S in the phase separated region. In homopolyelectrolyte coacervates, it has been shown in theory,[39,51,56,63,66–68] simulation,[40,41,66–68,100] and experiment[40,41] that salt can partition differently into the polyelectrolyte-dense coacervate phase and the polyelectrolyte-dilute supernatant phase. Recent work has also demonstrated that, when a neutral polymer is present, salt can accumulate at the interface between the supernatant and coacervate phase.[67] We investigate the distribution of salt in the nanophase separated structures seen in BCPE self-assembly by plotting a normalized salt concentration $\phi_S(\mathbf{r})/\langle\phi_S\rangle$ *versus* $\phi_A(\mathbf{r})$ for the points indicated in Fig. 5 at a variety of $\langle\phi_S\rangle$ and $\langle\phi_P\rangle$, in Fig. 6a–c and e. We distinguish the local values of $\phi_S(\mathbf{r})$ and $\phi_A(\mathbf{r})$ that vary across a BCPE morphology from the averaged values $\langle\phi_S\rangle$ and $\langle\phi_P\rangle$ that are the overall salt and polymer concentrations.

The end points of the curves in Fig. 6a–c and e represent the $\phi_S(\mathbf{r})/\langle\phi_S\rangle$ values in the most polymer-dense and polymer-dilute regions of the nanophase separated morphologies, and are analogous to the supernatant and coacervate phases in homopolyelectrolyte coacervation. We note that the normalized salt concentration corresponding to maximum-$\phi_A(\mathbf{r})$ values are significantly lower than the minimum-$\phi_A(\mathbf{r})$ values, consistent with the homopolyelectrolyte coacervate observation that salt typically partitions into the polymer-dilute phase.[39–41,66–68] To show that our results are consistent with salt partitioning to polymer-dilute regions in the block copolymer assembly, we also plot $\phi_P(\mathbf{r})/\langle\phi_P\rangle$ as a function of $\phi_A(\mathbf{r})$ in Fig. 6d and f, corresponding to Fig. 6c and e. The polymer-dilute regions indeed correspond to the salt-dense regions, and *vice versa*. This partitioning decreases noticeably as the overall salt concentration $\langle\phi_S\rangle$ increases, commensurate with a decrease in the variation in $\phi_A(\mathbf{r})$, again consistent with homopolyelectrolyte coacervates.[40,41,66–68]

The curves linking the two extreme values of $\phi_A(\mathbf{r})$ demonstrate how salt concentration changes across the interface between the phase separated domains. Low values of $\langle\phi_P\rangle$ (Fig. 6a) exhibit a mostly-monotonic decrease in $\phi_S(\mathbf{r})$, but even modest increases in $\langle\phi_P\rangle$ (Fig. 6b–d) lead to a non-monotonic behavior where a peak in $\phi_S(\mathbf{r})$ appears at intermediate $\phi_A(\mathbf{r})$. This is the accumulation of salt at the interface between the A and B blocks, consistent with prior predictions for homopolymer coacervates;[67] added neutral polymer partitions preferentially to the supernatant phase and leads to an interfacial excess of salt. This interfacial excess of salt increases with $\langle\phi_P\rangle$, and is most prominent at low values of $\langle\phi_S\rangle$. This can be attributed to the decrease in local overall polymer density at this position along the interface, now including both the charged A and neutral B species.

3.4 Extension of TM-SCFT calculation of charge-driven assembly to three-dimensions

We consider the two-dimensional phase diagrams presented here to be sufficient to show the primary trends associated with

 This journal is © The Royal Society of Chemistry 2019

Published on 06 June 2019. Downloaded by University of Illinois - Urbana on 1/28/2020 3:37:06 PM.

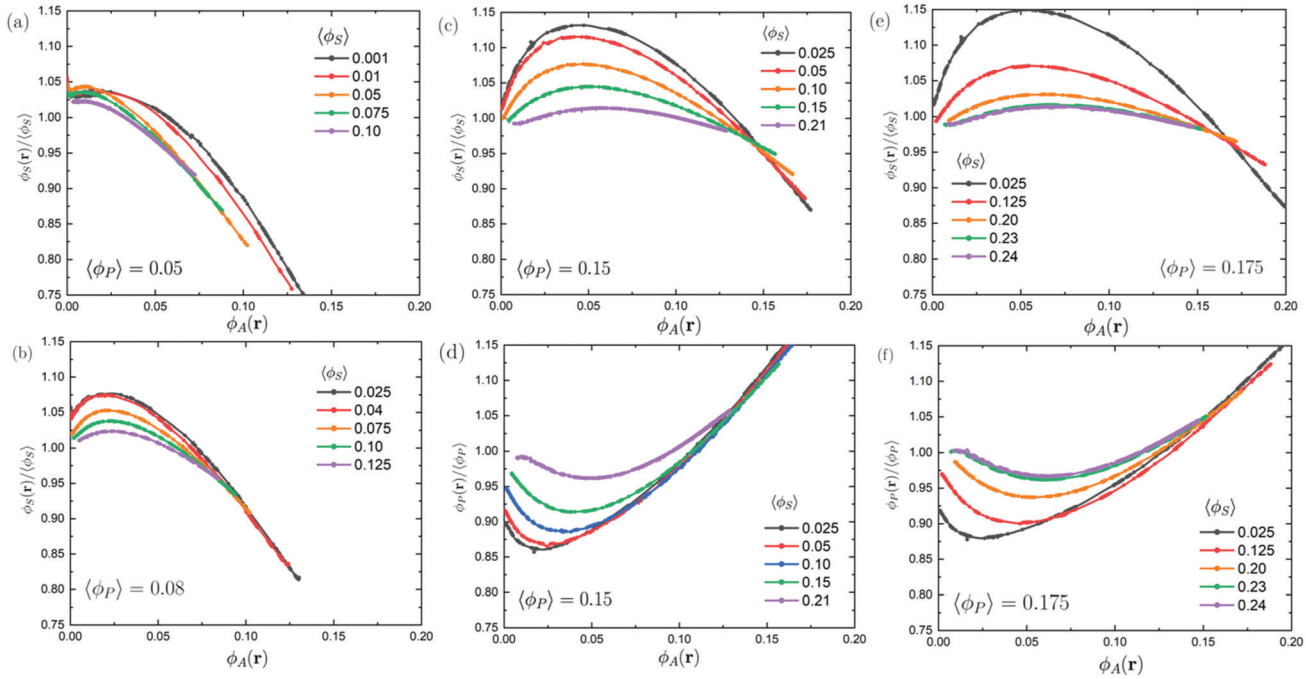

Fig. 6 Salt partitioning presented *via* the normalized salt concentration $\phi_S(\mathbf{r})/\langle\phi_S\rangle$ *versus* concentration of charged block $\phi_A(\mathbf{r})$ at each grid point for a given SCFT calculation for 30/30. Each subfigure represents the spatial distribution of salt concentration relative to the polyelectrolyte concentration at fixed overall polymer concentration ((a) $\langle\phi_P\rangle = 0.05$, (b) $\langle\phi_P\rangle = 0.075$, (c) $\langle\phi_P\rangle = 0.15$, (e) $\langle\phi_P\rangle = 0.175$). The effect of increasing salt concentration $\langle\phi_S\rangle$ while keeping polymer concentration constant is illustrated by the change in color. The corresponding concentration for every line is denoted in the phase diagram in Fig. 5(c). For (c) and (e), we also plot in (d) and (f) respectively the normalized total polymer concentration $\phi_P(\mathbf{r})/\langle\phi_P\rangle = (\phi_A(\mathbf{r}) + \phi_B(\mathbf{r}))/(\langle\phi_A\rangle + \langle\phi_B\rangle)$ for the same values of $\langle\phi_S\rangle$ and $\langle\phi_P\rangle$, to demonstrate that salt partitions preferentially to regions with low polymer density.

coacervate-driven self-assembly. Nevertheless, it is possible to extend the TM-SCFT method to three-dimensional space, so that a more diverse range of morphologies can be observed. In Fig. 7 we plot example morphologies from simulations performed in cubic boxes for the 40/20 case. These are initialized with field perturbations that are spatially-varying based on the eventual morphology, to minimize the amount of defects.[35,101,102] We then determine that these are the equilibrium structures by initializing the SCFT calculation with competing morphologies to ensure the ones reported are at the lowest free energy $\mathscr{H}^*$. We denote on the 2-D phase diagram from Fig. 3d the series of points ϕ_S and ϕ_A where we obtain these morphologies, and show that they roughly correspond to the two-dimensional phase diagram. We do see a wider range of morphologies, including BCC, hexagonal cylinders, gyroid, and lamellar structures. We note that we limit our investigation to 'classical' structures (BCC, cylinders, gyroid, lamellar), but it is possible that other phases could be observed as in uncharged block copolymers,[103–105]

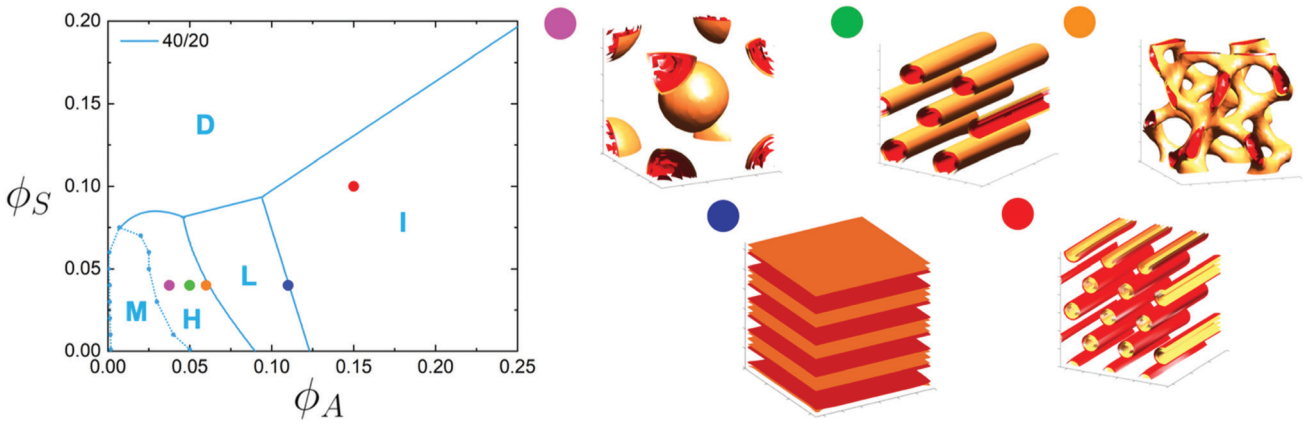

Fig. 7 Representative 3-D morphologies using TM-SCFT. We indicate on the 2-D, 40/20 phase diagram (Fig. 3d) the location of a number example points where we have calculated 3-D morphologies. We can see a wide range of classical block copolymer morphologies, including BCC, cylindrical, gyroid structures. We note that the location of these phases is consistent with prior work on uncharged block copolymer solutions.[81–83]

Published on 06 June 2019. Downloaded by University of Illinois - Urbana on 1/28/2020 3:37:06 PM.

especially in the presence of the third salt component. However, the ordering of this expanded list of morphologies once again demonstrates consistency with experimental phase diagrams for uncharged block copolymers,[81–83] with the BCC, cylindrical, and gyroid phases all existing in a relatively small region of ϕ_A space.

4 Conclusion

We are able to map the phase behavior of oppositely-charged diblock BCPEs that undergo coacervate-driven self-assembly. This was performed for a wide range of parameters, including charge fraction N_A/N_B, polymer length N, and salt and polymer concentrations ϕ_S and ϕ_P. We observe phase behaviors similar to standard χ-based block copolymer self-assembly,[81–83] only the salt concentration ϕ_S plays an analogous role to temperature in weakening the strength of interactions driving assembly. The local salt concentration can vary over the morphology, either by depleting from the polyelectrolyte-rich regions and/or by localizing at the block copolyelectrolyte interface.

These predictions set the stage for further theoretical and experimental investigation of coacervate-forming BCPEs. This model includes theoretical limitations that are fully articulated in our prior work,[66–68] and improvement of these methods – along with extension to three-dimensional calculations – will refine the ability to predict phase behavior. This method also provides a route to consider micelle stability and shape in analogy to the literature for uncharged block copolymers,[106–110] and can consider the inclusion of different architectures or more blocks. Finally, these predictions provide a first glimpse of the phase behavior expected of coacervate-forming diblock BCPEs, and can inform experimental design of these materials; however, beyond consistency of these results with existing experimental literature, experimental comparison remains necessary to fully test and refine the model.

Conflicts of interest

There are no conflicts to declare.

Appendix: transfer matrix theory

Our previous work has demonstrated how coacervation can be modeled by mapping the local charge correlations in a dense coacervate phase, which are largely associated with neighboring charges, to a one-dimensional adsorption model.[13,66–68] The solution of this adsorption model is carried out using the transfer matrix (TM) formalism, and provides predictions for both the macroscopic phase behavior and microscopic charge correlations present in complex coacervates.[13,66–68] A detailed exposition of this theory was published previously, including comparisons to simulation and experiment.[13,66–68]

In the TM theory, we consider a single test polyelectrolyte, where each charged monomer represents a single adsorption site along the contour of the polymer chain. We specifically consider polyelectrolytes in the high charge-density limit, such that most adsorption sites are associated or 'paired' with an oppositely-charged species. In this limit, the monomer concentration in coacervates is typically on the order of *ca.* 1 − 3M, and local charge correlations govern coacervate thermodynamics. This contrasts with the low charge-density limit, where field theoretic[25,42–47] or scaling theories[33,57–59] are well suited to capture longer-range charge and polymer fluctuations.

For this high charge-density adsorption model framework, the species adsorbed on to the test polyelectrolyte could be a small-molecule ion, S or a polyelectrolyte of the opposite charge, P′ or P, with an apostrophe denoting the first adsorbed polyelectrolyte monomer along a 'run' of sequentially-adsorbed monomers. There is also a possibility that the monomer adsorption site is vacant, representing an unpaired monomer 0. The grand-canonical partition function for this one-dimensional adsorption is:

$$\Xi = \vec{\psi}_0^{\mathrm{T}} \mathbf{M}^{N-1} \vec{\psi}_1 \tag{4}$$

Here, the vector $\vec{\psi}_1$ is a column vector of the Boltzmann factors for the states S, P′, P, and 0, while $\vec{\psi}_0$ is a vector of ones. The transfer matrix $\mathbf{M}$ is the transfer matrix, raised to the $N-1$ power to indicate the enumeration of the Boltzmann factors of N adsorption sites. The matrix $\mathbf{M}$ collects these Boltzmann factors *via* the form:

$$\mathbf{M}(s_i, s_{i-1}) = \begin{bmatrix} \mathrm{SS} & \mathrm{SP} & \mathrm{SP}' & \mathrm{S0} \\ \mathrm{PS} & \mathrm{PP} & \mathrm{PP}' & \mathrm{P0} \\ \mathrm{P}'\mathrm{S} & \mathrm{P}'\mathrm{P} & \mathrm{P}'\mathrm{P}' & \mathrm{P}'0 \\ 0\mathrm{S} & 0\mathrm{P} & 0\mathrm{P}' & 00 \end{bmatrix} = \begin{bmatrix} A & A & A & A \\ 0 & E & 2E & 0 \\ B & B & B & B \\ D & D & D & D \end{bmatrix} \tag{5}$$

Each term in the matrix is the Boltzmann factor associated with an adsorbed species at monomer s_i, given that the previous monomer was in the adsorption state s_{i-1}. We assign the factors $A = e^{\tilde{\mu}_S}$, $B = e^{\tilde{\mu}_P}$, and $D = e^{-\tilde{\varepsilon}}$, where tildes denote normalization by the thermal energy k_BT. The chemical potentials $\tilde{\mu}_S$ and $\tilde{\mu}_P$ are for the salt ions and monomer ions respectively, and capture the driving force for adsorption based on the environment of the test chain $\langle\phi_S\rangle$ and $\langle\phi_P\rangle$. We use expressions for A and B that arise from simple forms of the chemical potentials $\tilde{\mu}_S = \tilde{\mu}_S^0 + \ln\phi_S = \ln(A_0\phi_S)$ and $\tilde{\mu}_P = \tilde{\mu}_P^0 + \ln\phi_A = \ln(B_0\phi_A)$. $\tilde{\mu}_S^0$ and $\tilde{\mu}_P^0$ are reference chemical potentials for the salt and polyelectrolyte, and $A_0 = \exp\tilde{\mu}_S^0$ and $B_0 = \exp\tilde{\mu}_P^0$. $\tilde{\varepsilon}$ is a fitting parameter that captures the electrostatic penalty for an unpaired adsorption site, with most ions being paired due to the driving force for charge condensation along the chain. For this work, we assume that $e^{-\tilde{\varepsilon}} = 0$ for all ϕ_P and ϕ_S, indicating full charge pairing. This could be relaxed, though we expect only minor quantitative differences due to this simplifying assumption. Finally, E is the single-monomer partition function describing the confinement of subsequently-adsorbed monomers in a 'run' of an adsorbed polyelectrolyte. We are free to choose $E = 1$, because the matrix can be arbitrarily multiplied by a constant.

 This journal is © The Royal Society of Chemistry 2019

Published on 06 June 2019. Downloaded by University of Illinois - Urbana on 1/28/2020 3:37:06 PM.

Eqn (4) is analytically solvable by assuming the largest eigenvalue ξ dominates the partition function:

$$\Xi \approx \xi^N = \left[A + B + D + E. + \sqrt{(A + B + D + E)^2 - 4E(A - B + D)}\Big/2\right]^N \quad (6)$$

We use this result to calculate a free energy of interaction, F_{TM} between oppositely-charged polyelectrolytes:

$$\frac{F_{TM}}{Vk_BT} = -\frac{\phi_A}{2}\ln\xi \quad (7)$$

The excess free energy of the system, $F_{TM}/(Vk_BT) = \tilde{f}_{TM}$, can be calculated using eqn (7) with a phenomenological expression capturing the excluded volume of the non-water species to yield eqn (1):[66,68]

$$\frac{F_{EXC}}{Vk_BT} = \tilde{f}_{TM} = -\frac{\phi_A}{2}\ln\xi + \zeta(\Lambda(\phi_A + \phi_B) + \phi_S)^3 \quad (8)$$

ζ determines the strength of the excluded volume interaction, and $\Lambda = 0.6875$ accounts for the smaller excluded volume of the polymer relative to the salt ions.[68] The excess chemical potential fields $W_i(\{\phi_j\})$ were derived in our previous work,[67] and are the inputs to the SCFT portion of the calculation. Parameters used in this manuscript are $A_0 = 20.5$, $B_0 = 12.2$, and $\kappa = 19.0$ consistent with previous work.[68]

Acknowledgements

The authors thank careful reading and input from T. K. Lytle. The authors also acknowledge support by the National Science Foundation under Grant No. DMR-1654158.

References

1 H. G. Bungenberg de Jong and H. R. Kruyt, *Proc. Koninklijke Nederlandse Akademie Wetenschappen*, 1929, **32**, 849–856.
2 J. van der Gucht, E. Spruijt, M. Lemmers and M. A. Cohen Stuart, *J. Colloid Interface Sci.*, 2011, **361**, 407–422.
3 S. Srivastava and M. V. Tirrell, *Advances in Chemical Physics*, John Wiley and Sons, Hoboken, NJ, 2016.
4 C. E. Sing, *Adv. Colloid Interface Sci.*, 2017, **239**, 2–16.
5 D. Priftis and M. Tirrell, *Soft Matter*, 2012, **8**, 9396–9405.
6 S. L. Perry, Y. Li, D. Priftis, L. Leon and M. Tirrell, *Polymers*, 2014, **6**, 1756–1772.
7 E. Spruijt, A. H. Westphal, J. W. Borst and M. A. Cohen Stuart, *Macromolecules*, 2010, **43**, 6476–6484.
8 A. B. Marciel, S. Srivastava and M. V. Tirrell, *Soft Matter*, 2018, **14**, 2454–2464.
9 V. S. Rathee, A. J. Zervoudakis, H. Sidky, B. J. Sikora and J. K. Whitmer, *J. Chem. Phys.*, 2018, **148**, 114901.
10 K. I. Tainaka, *Biopolymers*, 1980, **19**, 1289–1298.
11 J. Fu and J. B. Schlenoff, *J. Am. Chem. Soc.*, 2016, **138**, 980–990.
12 L.-W. Chang, T. K. Lytle, M. Radhakrishna, J. J. Madinya, J. Velez and C. E. Sing, *Nat. Commun.*, 2017, **8**, 1273.
13 T. K. Lytle, L.-W. Chang, N. Markiewicz, S. L. Perry and C. E. Sing, *ACS Cent. Sci.*, 2019, **5**, 709–718.
14 S. L. Perry, L. Leon, K. Q. Hoffmann, M. J. Kade, D. Priftis, K. A. Black, D. Wong, R. A. Klein, C. F. Pierce III, K. O. Margossian, J. K. Whitmer, J. Qin, J. J. de Pablo and M. Tirrell, *Nat. Commun.*, 2015, **6**, 6052.
15 K. Q. Hoffman, S. L. Perry, L. Leon, D. Priftis, M. Tirrell and J. J. de Pablo, *Soft Matter*, 2015, **11**, 1525–1538.
16 B. M. Johnston, C. W. Johnston, R. Letteri, T. K. Lytle, C. E. Sing, T. Emrick and S. L. Perry, *Org. Biomol. Chem.*, 2017, **15**, 7630–7642.
17 J. R. Vieregg, M. Lueckheide, A. B. Marciel, L. Leon, A. J. Bologna, J. R. Rivera and M. V. Tirrell, *J. Am. Chem. Soc.*, 2018, **140**, 1632–1638.
18 P. Zhang, N. M. Alsaifi, J. Wu and Z.-G. Wang, *J. Chem. Phys.*, 2018, **149**, 163303.
19 M. A. Cohen Stuart, N. A. M. Besseling and R. G. Fokkink, *Langmuir*, 2004, **20**, 2785–2791.
20 A. Harada and K. Kataoka, *Macromolecules*, 1995, **28**, 5294–5299.
21 D. V. Pergushov, A. H. E. Müller and F. H. Schacher, *Chem. Soc. Rev.*, 2012, **41**, 6888–6901.
22 D. V. Krogstad, S.-H. Choi, N. A. Lynd, D. J. Audus, S. L. Perry, J. D. Gopez, C. J. Hawker, E. J. Kramer and M. V. Tirrell, *J. Phys. Chem.*, 2014, **118**, 13011–13018.
23 D. V. Krogstad, N. A. Lynd, D. Miyajima, J. Gopez, C. J. Hawker, E. J. Kramer and M. V. Tirrell, *Macromolecules*, 2014, **47**, 8026–8032.
24 D. V. Krogstad, N. A. Lynd, S.-H. Choi, J. M. Spruell, C. J. Hawker, E. J. Kramer and M. V. Tirrell, *Macromolecules*, 2013, **46**, 1512–1518.
25 D. J. Audus, J. D. Gopez, D. V. Krogstad, N. A. Lynd, E. J. Kramer, C. J. Haker and G. H. Fredrickson, *Soft Matter*, 2015, **11**, 1214–1225.
26 M. A. Cohen Stuart, N. A. M. Besseling and R. G. Fokkink, *Langmuir*, 1998, **14**, 6846–6849.
27 I. K. Voets, A. de Keizer and M. A. Cohen Stuart, *Adv. Colloid Interface Sci.*, 2009, **147**, 300–318.
28 H. M. van der Kooij, E. Spruijt, I. K. Voets, R. G. Fokkink, M. A. Cohen Stuart and J. van der Gucht, *Langmuir*, 2012, **28**, 14180–14191.
29 W. Blocher and S. Perry, *Wiley Interdiscip. Rev.: Nanomed. Nanobiotechnol.*, 2016, **9**, e1442.
30 S. Srivastava, M. Andreev, A. E. Levi, D. J. Goldfeld, J. Mao, W. T. Heller, J. J. de Pablo and M. V. Tirrell, *Nat. Commun.*, 2017, **8**, 14131.
31 H. Wu, J. M. Ting, O. Werba, S. Meng and M. V. Tirrell, *J. Chem. Phys.*, 2018, **149**, 163330.
32 J. M. Ting, H. Wu, A. Herzog-Arbeitman, S. Srivastava and M. V. Tirrell, *ACS Macro Lett.*, 2018, **7**, 726–733.
33 A. M. Rumyantsev, E. B. Zhulina and O. V. Borisov, *ACS Macro Lett.*, 2018, **7**, 811–816.
34 L. Leibler, H. Orland and J. C. Wheeler, *J. Chem. Phys.*, 1983, **79**, 3550–3557.

Published on 06 June 2019. Downloaded by University of Illinois - Urbana on 1/28/2020 3:37:06 PM.

35 L. Leibler, *Macromolecules*, 1980, **13**, 1602–1617.
36 A. Halperin, *Macromolecules*, 1987, **20**, 2943–2946.
37 I. Michaeli, J. T. G. Overbeek and M. J. Voorn, *J. Polym. Sci.*, 1957, **23**, 443–449.
38 J. T. G. Overbeek and M. J. Voorn, *J. Cell. Comp. Physiol.*, 1957, **49**, 7–26.
39 S. L. Perry and C. E. Sing, *Macromolecules*, 2015, **48**, 5040–5053.
40 M. Radhakrishna, K. Basu, Y. Liu, R. Shamsi, S. L. Perry and C. E. Sing, *Macromolecules*, 2017, **50**, 3030–3037.
41 L. Li, S. Srivastava, M. Andreev, A. B. Marciel, J. J. de Pablo and M. V. Tirrell, *Macromolecules*, 2018, **51**, 2988–2995.
42 J. Lee, Y. O. Popov and G. H. Fredrickson, *J. Chem. Phys.*, 2008, **128**, 224908.
43 R. A. Riggleman, R. Kumar and G. H. Fredrickson, *J. Chem. Phys.*, 2012, **136**, 024903.
44 Q. Wang, T. Taniguchi and G. H. Fredrickson, *J. Phys. Chem. B*, 2004, **108**, 6733–6744.
45 A.-C. Shi and J. Noolandi, *Macromol. Theory Simul.*, 1999, **8**, 214–229.
46 K. T. Delaney and G. H. Fredrickson, *J. Chem. Phys.*, 2017, **146**, 224902.
47 S. P. O. Danielsen, J. McCarty, J.-E. Shea, K. Delaney and G. Fredrickson, *Proc. Natl. Acad. Sci. U. S. A.*, 2019, **116**, 8224–8232.
48 V. Y. Borue and I. Y. Erukhimovich, *Macromolecules*, 1990, **23**, 3625–3632.
49 M. Castelnovo and J. F. Joanny, *Eur. Phys. J. E: Soft Matter Biol. Phys.*, 2001, **1**, 203–214.
50 P. M. Biesheuvel and M. A. Cohen Stuart, *Langmuir*, 2004, **20**, 2785–2791.
51 A. Kudlay and M. O. de la Cruz, *J. Chem. Phys.*, 2004, **120**, 404–412.
52 A. Kudlay, A. V. Ermoshkin and M. O. de la Cruz, *Macromolecules*, 2004, **37**, 9213–9241.
53 J. Qin and J. J. de Pablo, *Macromolecules*, 2016, **49**, 8789–8800.
54 A. M. Rumyantsev, E. Y. Kramarenko and O. V. Borisov, *Macromolecules*, 2018, **51**, 6587–6601.
55 K. Shen and Z.-G. Wang, *Macromolecules*, 2018, **51**, 1706–1717.
56 P. Zhang, K. Shen, N. M. Alsaifi and Z.-G. Wang, *Macromolecules*, 2018, **51**, 5586–5593.
57 Z. Wang and M. Rubinstein, *Macromolecules*, 2006, **39**, 5897–5912.
58 A. M. Rumyantsev, E. B. Zhulina and O. V. Borisov, *Macromolecules*, 2018, **51**, 3788–3801.
59 M. Rubinstein, Q. Liao and S. Panyukov, *Macromolecules*, 2018, **51**, 9572–9588.
60 R. Zhang and B. I. Shklovskii, *Physica A*, 2005, **352**, 216–238.
61 A. Salehi and R. G. Larson, *Macromolecules*, 2016, **49**, 9706–9719.
62 S. Friedowitz, A. Salehi, R. G. Larson and J. Qin, *J. Chem. Phys.*, 2018, **149**, 163335.
63 S. Adhikari, M. A. Leaf and M. Muthukumar, *J. Chem. Phys.*, 2018, **149**, 163308.
64 M. Muthukumar, *Macromolecules*, 2017, **50**, 9528–9560.
65 M. Radhakrishna and C. E. Sing, *Macromol. Chem. Phys.*, 2016, **217**, 126–136.
66 T. K. Lytle and C. Sing, *Mol. Syst. Des. Eng.*, 2018, **3**, 183–196.
67 T. K. Lytle, A. J. Salazar and C. E. Sing, *J. Chem. Phys.*, 2018, **149**, 163315.
68 T. K. Lytle and C. E. Sing, *Soft Matter*, 2017, **13**, 7001–7012.
69 M. T. Record, C. F. Anderson and T. M. Lohman, *Q. Rev. Biophys.*, 1978, **11**, 103–178.
70 G. S. Manning, *J. Chem. Phys.*, 1969, **51**, 924–933.
71 Z. Ou and M. Muthukumar, *J. Chem. Phys.*, 2006, **124**, 154902.
72 R. M. Elder, T. Emrick and A. Jayaraman, *Biomacromolecules*, 2011, **12**, 3870–3879.
73 R. S. Dias, P. Linse and A. A. C. C. Pais, *J. Comput. Chem.*, 2011, **32**, 2697–2707.
74 R. M. Elder and A. Jayaraman, *Macromolecules*, 2012, **45**, 8083–8096.
75 H. S. Antila, M. Harkonen and M. Sammalkorpi, *Phys. Chem. Chem. Phys.*, 2015, **17**, 5279–5289.
76 B. Peng and M. Muthukumar, *J. Chem. Phys.*, 2015, **143**, 243133.
77 E. Raspaud, M. O. de la Cruz, J. L. Sikorav and F. Livolant, *Biophys. J.*, 1998, **74**, 381–393.
78 M. O. de la Cruz, L. Belloni, M. Delsanti, J. P. Dalbiez, O. Spalla and M. Drifford, *J. Chem. Phys.*, 1995, **103**, 5781–5791.
79 B. K. Brettmann, N. Laugel, N. Hoffmann, P. Pincus and M. Tirrell, *J. Polym. Sci., Part A: Polym. Chem.*, 2016, **54**, 284–291.
80 B. Brettmann, P. Pincus and M. Tirrell, *Macromolecules*, 2017, **50**, 1225–1235.
81 T. P. Lodge, K. J. Hanley, B. Pudil and V. Alahapperuma, *Macromolecules*, 2003, **36**, 816–822.
82 T. P. Lodge, B. Pudil and K. J. Hanley, *Macromolecules*, 2002, **35**, 4707–4717.
83 C. Lai, W. B. Russel and R. A. Register, *Macromolecules*, 2002, **35**, 841–849.
84 J. Lou, S. Friedowitz, J. Qin and Y. Xia, *ACS Cent. Sci.*, 2019, **5**, 549–557.
85 G. Fredrickson, *The Equilibrium Theory of Inhomogeneous Polymers*, Oxford University Press, 2013.
86 I. Nakamura and Z.-G. Wang, *Soft Matter*, 2013, **9**, 5686–5690.
87 K. Shull, *Macromolecules*, 1992, **25**, 2122–2133.
88 K. R. Shull and E. J. Kramer, *Macromolecules*, 1990, **23**, 4769–4779.
89 H. D. Ceniceros and G. H. Fredrickson, *Multiscale Model. Simul.*, 2004, **2**, 452–474.
90 A. Levy, D. Andelman and H. Orland, *Phys. Rev. Lett.*, 2012, **108**, 227801.
91 Y.-Z. Wei, P. Chiang and S. Sridhar, *J. Chem. Phys.*, 1992, **96**, 4569–4573.
92 Z.-G. Wang, *Phys. Rev. E: Stat., Nonlinear, Soft Matter Phys.*, 2010, **81**, 021501.

 This journal is © The Royal Society of Chemistry 2019

Published on 06 June 2019. Downloaded by University of Illinois - Urbana on 1/28/2020 3:37:06 PM.

93 Y. Yan, A. de Keizer, M. A. Cohen Stuart, M. Drechsler and N. A. M. Besseling, *J. Phys. Chem. B*, 2008, **112**, 10908–10914.
94 M. W. Matsen and F. S. Bates, *Macromolecules*, 1996, **29**, 7641–7644.
95 F. S. Bates and G. H. Fredrickson, *Annu. Rev. Phys. Chem.*, 1990, **41**, 525–557.
96 M. W. Matsen and F. S. Bates, *Macromolecules*, 1996, **29**, 1091–1098.
97 P. J. Flory, *Principles of Polymer Chemistry*, Cornell University Press, Ithaca, NY, 1953.
98 C.-I. Huang and T. P. Lodge, *Macromolecules*, 1998, **31**, 3556–3565.
99 J. R. Naughton and M. W. Matsen, *Macromolecules*, 2002, **35**, 5688–5696.
100 M. Andreev, V. M. Prabhu, J. F. Douglas, M. V. Tirrell and J. J. de Pablo, *Macromolecules*, 2018, **51**, 6717–6723.
101 S. Qi and Z.-G. Wang, *Phys. Rev. E: Stat. Phys., Plasmas, Fluids, Relat. Interdiscip. Top.*, 1997, **55**, 1682–1697.
102 D. A. Hajduk, P. E. Harper, S. M. Gruner, C. C. Honeker, G. Kim, E. L. Thomas and L. J. Fetters, *Macromolecules*, 1994, **27**, 4063–4075.
103 S. Lee, M. J. Bluemle and F. S. Bates, *Science*, 2010, **330**, 349–353.
104 S. Lee, C. Leighton and F. S. Bates, *Proc. Natl. Acad. Sci. U. S. A.*, 2014, **111**, 17723–17731.
105 M. Liu, Y. Qiang, W. Li, F. Qiu and A.-C. Shi, *ACS Macro Lett.*, 2016, **5**, 1167–1171.
106 G. A. McConnell and A. P. Gast, *Phys. Rev. E: Stat. Phys., Plasmas, Fluids, Relat. Interdiscip. Top.*, 1996, **54**, 5447–5455.
107 V. G. de Bruijn, L. J. P. van den Broeke, F. A. M. Leermakers and J. T. F. Keurentjes, *Langmuir*, 2002, **18**, 10467–10474.
108 J. Zhou and A.-C. Shi, *Macromol. Theory Simul.*, 2011, **20**, 690–699.
109 F. A. M. Leermakers, C. M. Wijmans and G. J. Fleer, *Macromolecules*, 1995, **28**, 3434–3443.
110 P. N. Hurter, J. M. H. M. Scheutjens and T. A. Hatton, *Macromolecules*, 1993, **26**, 5592–5601.